Eurographics Workshop on Visual Computing for Biology and Medicine (2016)
S. Bruckner, B. Preim, and A. Vilanova (Editors)

Temporal interpolation of 4D PC-MRI blood-flow measurements using bidirectional physics-based fluid simulation

N.H.L.C. de Hoon[1], A.C. Jalba[2], E. Eisemann[1] and A. Vilanova[1]

[1]Electrical Engineering, Mathematics and Computer Science, Delft University of Technology, The Netherlands
[2]Computer Science and Mathematics, Eindhoven University of Technology, The Netherlands

Abstract

Magnetic Resonance Imaging (MRI) enables volumetric and time-varying measurements of blood-flow data. Such data have shown potential to improve diagnosis and risk assessment of various cardiovascular diseases. Hereby, a unique way of analysing patient-specific haemodynamics becomes possible. However, these measurements are susceptible to artifacts, noise and a coarse spatio-temporal resolution. Furthermore, typical flow visualization techniques rely on interpolation. For example, using pathlines requires a high quality temporal resolution. While numerical simulations, based on mathematical flow models, address some of these limitations, the involved modelling assumptions (e.g., regarding the inflow and mesh) do not provide patient-specific data to the degree actual measurements would. To overcome this issue, data assimilation techniques can be applied to use measured data in order to steer a physically-based simulation of the flow, combining the benefits of measured data and simulation. Our work builds upon such an existing solution to increase the temporal resolution of the measured data, but achieves significantly higher fidelity. We avoid the previous damping and interpolation bias towards one of the measurements, by simulating bidirectionally (forwards and backwards through time) and using sources and sinks. Our method is evaluated and compared to the, currently-used, conventional interpolation scheme and forward-only simulation using measured and analytical flow data. It reduces artifacts, noise, and interpolation error, while being closer to laminar flow, as is expected for flow in vessels.

Categories and Subject Descriptors (according to ACM CCS): I.3.3 [Computer Graphics]: Applications—4D PC-MRI Blood-Flow I.6.8 [Simulation and Modelling]: Types of Simulation—Combined G.1.1 [Mathematics of Computing]: Numerical Analysis—Interpolation

1. Introduction

Cardiovascular diseases are worldwide the leading cause of death [MBG*15]. Hence, an understanding of these diseases can have a considerable impact. Traditionally, cardiovascular disease diagnosis and risk assessment is based on measurements of morphology observed with the aid of anatomical medical imaging. However, this ignores the blood flow itself, while it is known that blood flow influences the morphology and vice versa [HBB*10, MFK*12, MSW*16]. For a full analysis of the cardiovascular system, both knowledge of morphology and blood flow are essential. Visual exploration of flow data aids the understanding of this data [BMGS13, VPvP*14, VPvP*12, KGP*13, LGP14].

Flow data can be obtained using physical simulations [MNvTK*16], yielding noise- and artifact-free flow data. Often finite element methods (FEM) are used, which require a detailed mesh of the patients vessel morphology, as well as in- and outflow conditions. These are often obtained from measurements in patients. Nevertheless, simulations remain a model of the true flow, and are based on assumptions of the actual flow. This makes the results useful, although often insufficiently patient specific [DN15].

Additionaly, the velocity of the blood-flow can be acquired by using contemporary imaging modalities, such as Doppler ultrasound and Phase-Contrast Magnetic Resonance Imaging (PC-MRI). Of these techniques, although being less cost effective, only 4D PC-MRI yields unsurpassed complete information of volumetric velocity data over time. Acquisition of PC-MRI and its applications is described in detail by Markl et al. [MFK*12].

Despite the richness of information, the measurements are prone to noise and artifacts [MFK*12, MSW*16], as is the case for any measurement of physical behaviour. Besides, so-called phase-wrap artifacts, which are inherent to the way flow is measured and often corrected by tailored algorithms, motion artifacts occur especially in the vicinity of the moving cardiac and vessel walls. Also, the spatial resolution remains limited, leading to partial volume effects. This causes poorly defined velocity vectors near the walls, because boundary transitions occur at sub-voxel scale. One of the most pressing issues for the analysis is, however, the coarse tem-

© 2016 The Author(s)
Eurographics Proceedings © 2016 The Eurographics Association.

DOI: 10.2312/vcbm.20161272

delivered by EUROGRAPHICS DIGITAL LIBRARY www.eg.org diglib.eg.org

poral resolution. This temporal undersampling of PC-MRI makes it hard to identify the loss of fundamental flow or diagnostic information, such as the computation of the aortic pulse wave velocity [DHH*16], from the measured blood motion, especially for high velocity flow, such as in the aorta.

In this paper, we present a novel method based on the work by de Hoon et al. [dHvPJV14] for improving temporal resolution of PC-MRI data for flow visualizations. The method is based on the coupling of PC-MRI measurements and physics-based fluid simulations. We strive to improve the temporal interpolation of de Hoon et al. by taking both the previous and next measurement into account, opposed to only the previous measurement. Moreover, important flow features, such as vorticity, must remain present. To accomplish this, we simulate the flow from the next measurement backward in time. Furthermore, we counteract the damping effect observed by de Hoon et al. by introducing sources and sinks. To validate our method we use high-resolution measurements to compare our method with de Hoon et al., the current conventional interpolation scheme and measurements.

In summary, the main contributions of this paper are:

- a novel method based on the work by de Hoon et al. [dHvPJV14] for improving temporal interpolation for flow visualization.
- a reduction of the damping effect observed by de Hoon et al. by introducing sources and sinks.
- a validation of our method using high-resolution measurements, comparing our method with de Hoon et al. and the current conventional interpolation scheme.

2. Related work

Data assimilation is the process of combining observed (i.e., measured) data of a system with scientific information, typically a mathematical model of the system, to obtain an estimate of the true state of the system. That is, it attempts to use all available information of a system to estimate its true state. Hence, it can be used for interpolation and extrapolation of measured data. Multiple data assimilation techniques exist and are being used in many fields, such as meteorology [BEE*15], geoscience [RHJ*04], climatology [SBF*14].

In our case, we use 4D PC-MRI measurements and a physical model of blood flow, since the latter provides a full 4D velocity field. We choose to use a physics-based fluid simulation from the computer graphics field, because these are faster than common computation fluid dynamics (CFD) based models, but which are generally of higher accuracy. For visualization, we should aim at having real time interpolation, although, this is not the main focus of the paper at this point.

Data assimilation has been used in a similar context before [HMM*10, RMB*14, DPV12, AABDZ14]. However, none of these methods are applied to 4D PC-MRI measurements, and hence, do not provide a 3D flow field over time while being minimal invasive for the patient.

The method by de Hoon et al. [dHvPJV14] uses PC-MRI measurements. It takes the physical behaviour into account by means of a physics-based fluid simulation from the computer graphics field, yet, only a single measurement is used for the assimilation, resulting in a bias towards this measurement and generating discontinuous behaviour. This discontinuity will be further elaborated on in Section 5. A similar approach was proposed by Rispoli et al. [RNNC15], however, the method focusess on increasing the spatial resolution and denoising the individual PC-MRI measurements.

3. Bidirectional coupling for interpolation

This section first covers the flow simulation required for modelling blood flow. Then, the coupling of the measured data with the simulation is presented. This coupling is used to simulate blood flow both forward and backwards through time. The results of both simulations are then merged to yield to an interpolation that considers two time-step measurements rather than just using the initial one. Finally, fluid sources and sinks are introduced, which are used to reduce the undesired flow damping.

3.1. Blood-flow simulation

Blood is modelled as an incompressible inviscid fluid using the Navier-Stokes equations, given by

$$\frac{\partial \mathbf{u}}{\partial t} = -\mathbf{u}\cdot\nabla\mathbf{u} - \frac{1}{\rho}\nabla p \tag{1}$$

$$\nabla\cdot\mathbf{u} = 0, \tag{2}$$

where $\mathbf{u}^t(\mathbf{x})$ is the fluid velocity at position $\mathbf{x}$ and time step t, $p^t(\mathbf{x})$ is the pressure and ρ is the density. In the remainder of this paper, where possible, the position $\mathbf{x}$ and time step t will be obmitted. The rate of change of fluid per unit volume is given by the velocity divergence ($\nabla\cdot\mathbf{u}$), thus Equation (2) constrains the velocity field to be divergence-free, i.e., incompressible.

Note that, Equation (1) does not contain the viscosity term $\frac{1}{\rho}\nabla\cdot(\mu(\nabla\mathbf{u}+(\nabla\mathbf{u})^T))$. The main reason for doing so is that the Navier-Stokes equation for incompressible, inviscid flow is time-reversible [DOW08], which is an essential requirement for our bidirectional coupling method. Indeed, since fluid viscosity is modelled as a diffusion process, i.e., a time-dependent process causing the momentum to change in space, time reversibility becomes an ill-posed problem. Many possible previous states exist, given an initial flow field. Although, it is common to neglect viscosity in computer graphics when simulating water [Bri08]. We use such a computer graphics simulation, described in the next paragraph, which inherently has numerical dissipation, that could be regarded as a viscous force on the flow. Viscous effects are small for high-speed blood flow in big vessels for this reason and for simplicity viscosity was also neglected in the work of de Hoon et al. [dHvPJV14]. However, close to the vessels walls viscosity is important. In order to still allow certain viscous behaviour of blood, we use the so-called 'no-slip' boundary condition. This Dirichlet-type boundary condition states, for viscous fluids, that the velocity of the fluid at a solid boundary is equal to the boundary's velocity, i.e., $\mathbf{u} = \mathbf{u}_{solid}$. For static boundaries, $\mathbf{u}_{solid} = 0$, thus $\mathbf{u} = 0$ at solid boundaries. This approach results thus in an approximate viscous flow, without the need of modelling viscosity explicitly in the Navier-Stokes equation.

Similar to de Hoon et al., we discretise Equations (1) and (2)

© 2016 The Author(s)
Eurographics Proceedings © 2016 The Eurographics Association.

applying the Fluid Implicit Particle (FLIP) method – a hybrid, Langrangian-Eulerian approach – using particles and an auxiliary grid. Particles preserve small-scale flow features and ensure low numerical dissipation, whereas the grid is used to modify the particle velocities due to the pressure term. For more details on the FLIP method see Zhu et al. [ZB05]. To ensure that no empty grid cells exist, i.e., no air cells where there should be fluid, we inject additional particles in those cells. By the Courant-Frederichs-Lewy (CFL) condition, which states that the time step should be such that a particle can move at most one cell per iteration, empty cells can only occur next to fluid cells. Thus, the velocity of these new particles is derived from the so-called extended velocity field, computed using the sweeping method of Zhao [Zha05].

3.2. Backward simulation

Our technique requires the use of a flow model that is time reversible. That is, if $\mathbf{u}^n(\mathbf{x})$ is the solution at time step t^n, given the initial condition $\mathbf{u}^0(\mathbf{x})$. Then time-reversibility means that it is possible to go from $\mathbf{u}^n(\mathbf{x})$ back to $\mathbf{u}^0(\mathbf{x})$ after n steps. Given that Equation (1) is time reversible (see, e.g., Duponchee et al. [DOW08]), we proceed as follows. The simulation is run until a certain time t^n is reached (forward simulation), after which the time is reversed. Time reversal is simply obtained by switching the sign of the velocity field, as is demonstrated by Duponchee et al. [DOW08]. The simulation is then run again from $-\mathbf{u}^n(\mathbf{x})$ to $-\mathbf{u}^0(\mathbf{x})$ for the same number of time steps as before (backwards simulation), so that an ideal solver would recover the sign-reversed initial condition. Note that, after the backwards simulation one needs to reverse again the sign of of the velocity field, such that it points in the original direction.

3.3. Coupling measurements with simulation

Now that we have a fluid simulation in place, we have to assimilate the simulation with the measured data. Given a measured velocity field $\mathbf{u}_m^n$ and simulated velocity field $\mathbf{u}_s^n$ at time t^n, let $\mathbf{u}_d^n = \mathbf{u}_s^n - \mathbf{u}_m^n$ be the velocity difference between the simulation and measurement. Note that, if the measurement would be noise- and artifact-free and the simulation would be a perfect model, $\mathbf{u}_d^n$ would be $\mathbf{0}$, since both describe the same flow. The concept of the coupling introduced by de Hoon et al. [dHvPJV14] is to obtain a new simulation velocity field $\mathbf{u}_{new}^{n+1}$ such that $\mathbf{u}_{new}^{n+1} \leftarrow \mathbf{u}_s^{n+1} - \mathbf{u}_d^{n+1}$. The new velocity field will represent the measurements better, while maintaining the divergence-free properties of the simulation.

Since the measurements are of blood-flow, it is assumed that it also obeys the same momentum equation, i.e.,

$$\frac{\partial \mathbf{u}_m}{\partial t} = -\mathbf{u}_m \cdot \nabla \mathbf{u}_m. \tag{3}$$

Note that, the pressure terms are omitted, since they are unknown for measurements. Furthermore, since $\mathbf{u}_m$ is measured and therefore is prone to noise and artifacts, it may not be divergence free.

Now subtracting Equation (3), representing the measurements, from Equation (1), representing the simulation, one obtains

$$\frac{\partial \mathbf{u}_d}{\partial t} = -\mathbf{u}_s \cdot \nabla \mathbf{u}_s + \mathbf{u}_m \cdot \nabla \mathbf{u}_m - \frac{1}{\rho}\nabla p \tag{4}$$
$$\nabla \cdot \mathbf{u}_d = 0.$$

This equation can be solved for $\mathbf{u}_d^{n+1}$ using the fluid simulation method described in Section 3.1, yielding a divergence-free velocity field. We can then use this velocity field through $\mathbf{u}_{new}^{n+1} \leftarrow \mathbf{u}_s^{n+1} - \mathbf{u}_d^{n+1}$, to obtain the new divergence-free simulation velocity field.

3.3.1. Bidirectional simulation

Previous section described the coupling of the simulation with the measurements, whenever measured data is available for that time step. Therefore, the simulation is steered when a measurement is available. In between the measurements, the simulation provides intermediate velocity fields based on an initial measurement until the next measurement and the simulation gets coupled again. Note that, due the the coupling, the divergence free and no-slip boundary condition applies the measured time points and the intermediate velocity fields. However, when simulating only forward, the interpolation will be biased, towards one measurement in time, and not towards the two nearest measurements in time. This causes a discontinuity in time, when a measurement becomes available. To overcome this issue, we propose to also simulate backward in time, as described in Section 3.2. Doing so, for every point in time two velocity fields are obtained. Since both velocity fields are divergence-free, a weighted sum will result in another divergence-free velocity field. For best results, this weight should be related to the distance in time to the last coupling of the simulation, forward and backward respectively. The longer the simulation runs without coupling, the more it is likely to deviate from the measured flow, hence the lower the weight should be.

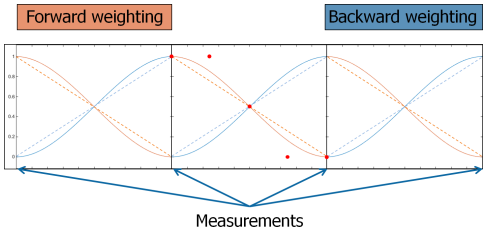

Figure 1: Using a smooth Bézier weighting (Equation (5)) for combining divergence-free velocity fields, yields a new divergence-free velocity field that is second-order continuous over time. The red dots indicate the 5 control points $(1, 1, \frac{1}{2}, 0, 0)$ for one of the fourth order Bézier curves ensuring C^1 continuity. The dashed lines indicate linear weighting, which is non-differentiable at the measurements.

A naive approach would be to use linear weighting, where a weight of one is assigned when the simulation is coupled and a weight of zero when another measurement is reached. However, using linear weights makes the weighting non-differentiable at the measurements, since the sign of the derivative is inverted. Hence, the derivative of the resulting velocity field over time, namely the acceleration, would not be continuous.

© 2016 The Author(s)
Eurographics Proceedings © 2016 The Eurographics Association.

We use a smooth one-dimensional, fourth order Bézier curve with uniformly distributed control points, see Figure 1, which results in a C^1 continious differentiable interpolation. After removal of the terms that evaluate to zero, gives us

$$B(t) = 3 \cdot t^2 \cdot (1-t)^2 + 4 \cdot t^3 \cdot (1-t) + t^4, \quad (5)$$

with $t \in [0,1]$ is the normalized time between two consecutive measurements, where $t = 0$ is the current measurement and $t = 1$ represents the next measurement. The resulting curves, $1 - B(t)$ for forward and $B(t)$ for backward simulation, are shown in Figure 1.

These curves produce the weighting that result in the desired second-order continuous transition over time of the velocity field, opposed to using a linear weighting, while maintaining a total weight of one. Hereby, the acceleration is enforced to be smooth throughout the time domain. Another advantage is that the nearest measurement has a higher weight compared to linear weighting. It is to be noted that other strategies, such as B-spline or Hermite splines, that result in a smooth weighting could also be studied.

3.3.2. Sources and sinks

Simulating fluid in a closed container makes that the PDE for pressure has no solution, due to the so-called compatibility condition. Simulating in such a container is thus more difficult and requires assumptions about the fluid, which may induce compressibility. To avoid using such limiting assumptions, de Hoon et al. [dHvPJV14] removed particles within a certain distance to the grid boundary. This ensures that a free surface always exists close to the grid boundary, i.e., a surface separating fluid and air, as opposed to fluid and solid. Therefore, the polygonal mesh should be constructed, such that no fluid is desired to be simulated close to the grid boundaries, which limits the latter method [dHvPJV14] to some extent. Furthermore, the amount of fluid simulated could be undesirably large, resulting in a higher computation time. We provide more flexible user-definable sources, where fluid enters the system, and sinks, where fluid exits the system, such that the free surface is always available and the user can define where fluid should be simulated. The placement of the sinks and sources depends on the region of interest to ensure it is covered by the simulation.

Sources are grid cells that emit fluid continuously. The velocity of the particles in these cells is obtained from the measurements and using linear interpolation in time. Notice that, also higher resolution 2D measurements could be used for this purpose. *Sinks* are cells for which all contained fluid particles are removed at every time step. Both, sources and sinks, shown in Figure 2, ensure that the fluid has a free surface, and thus, we do not simulate a fluid in a closed container. Note that the CFL condition, which limits a simulation time step to be such that a particle moves at most one cell per step, ensures that no particles overshoots a sink nor can a source be empty.

Fluid is initialized only in cells that are between a source and a sink cell, i.e., a cell contains fluid if and only if both, a source and a sink cell, are reachable without intersection of source, sink or solid cells – see the valid region in Figure 2. The only assumption is that the source and sink cells are always on a plane intersecting the solid, such that no fluid can leak through.

Finding cells, that should contain fluid, is achieved by using a sweeping algorithm. For every source and sink cell, a sweeping is started. The sweeping stops in a direction, if the cell reached is solid, source, sink or reachable by a cell with the same type, being either a source or a sink. In case a cell is reachable by another type, the cell is marked as valid and the sweep continues. The algorithm visits each cell at most three times, and can be performed as a preprocessing step after the source and sink cells are defined. Pseudo code for this sweeping algorithm is given in the additional materials.

Similar to de Hoon et al. [dHvPJV14], we add particles in empty cells that should contain fluid. If a measurement is available, the measured velocity is applied. Otherwise, we use the Fast Sweeping Method by Zhao [Zha05] to extend the fluid velocity field to these empty cells.

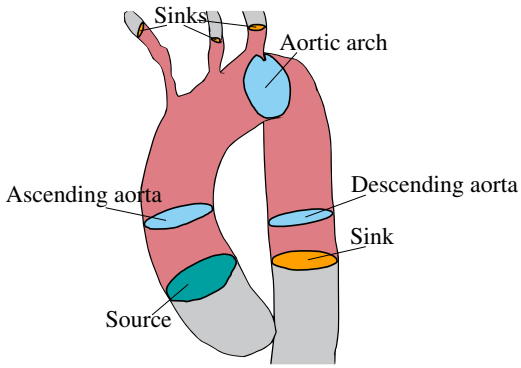

Figure 2: Using perpendicular disk-shaped sources (green) and sinks (orange), the user can select a valid region (pink area) in which to simulate. The lightblue disks indicate the used evaluation planes perpendicular to the mesh. These disks are placed in the ascending aorta, the aortic arch and the descending aorta.

4. Flow comparison

Due to the lack of a ground truth, validation and evaluation of the results is a challenge. In this paper, we will compare our results to a high temporal resolution PC-MRI acquisition. This data has a temporal resolution of 23ms, giving 46 phases for a heart cycle, while typically only 20 to 25 phases per cycle are acquired. We will also compare our results to previous methods: linear interpolation and de Hoon et al. [dHvPJV14] to analyse the differences.

For this purpose, we have to be able to compare two vector fields. Therefore, we developed multiple visualizations that help to analyse data sets both locally, as well as globally, in a qualitative and quantitative manner. We have multiple metrics on vector data sets, see Table 1 for an overview. Vector field $\mathbf{u}$ represents the given velocity field. Furthermore, $\mathbf{n}_s$ denotes the inward normal of the solid mesh, required for the wall shear stress (WSS) computation. Note that for an accurate calculation of WSS viscosity is relevant. However, an estimation of WSS is often calculated using PC-MRI measurements. An estimation of the viscosity is used as a constant value μ.

All these metrics represent different aspects of the flow that are of interest, either for blood-flow analysis (e.g. the WSS), or to show

© 2016 The Author(s)
Eurographics Proceedings © 2016 The Eurographics Association.

Metric	Computation
Velocity magnitude	$\|\|\mathbf{u}\|\|$
Curl magnitude	$\|\|\nabla \times \mathbf{u}\|\|$
Acceleration	$\left\|\left\|\frac{d}{dt}\mathbf{u}\right\|\right\|$
WSS magnitude	$\mu\|\|\nabla \mathbf{u} \cdot \mathbf{n}_s\|\|$

Table 1: Different metrics used for analysis of the vector field $\mathbf{u}$.

relevant general aspects of the flow. The *magnitude* of the flow on a plane is a representation of the amount of fluid that passes through that plane. It will, therefore, be used to compare the difference in flow, as well as in local speed. The *curl* of a vector field is the axis of rotation (vorticity). The magnitude of such a vector gives the local amount of vorticity. If there is curl at a point, the flow is not symmetric for that point. Globally, the more curl a flow shows, the more turbulent it is. *Acceleration* describes the change in velocity over time. Visualizing the acceleration helps to get more insight in the changes of the velocity field over time, which is important for understanding how a volume of fluid moves through the aorta, i.e., its advection. The *wall shear stress* (WSS) of a flow measures the shear stress the fluid exerts on the vessel wall. It is of clinical importance, since a high magnitude of WSS has been associated with cardiovascular diseases. Another interesting metric is the *divergence* of a vector field, which measures locally whether the vector field has sources or sinks apart from the input and output of the system, i.e., flow is respectively created or removed from the field. Note that for an incompressible fluid, like blood, the divergence should be zero, i.e., divergence-free. Thus, the flow does not contain sources nor sinks, excluding the ones defined by the user. In the simulated data divergence-free is imposed, so divergence will be zero everywhere. Yet, for the measured data it is known that this is not the case and it will not be zero everywhere.

Different qualitative visualizations are implemented to visualize the above metrics. One can select a disk intersecting the vessel wall to locally inspect the metrics. Furthermore, an iso-surface can be created to globally find regions that could be of interest, such as regions with high WSS. For direction and magnitude comparison of both velocity fields, one can visualize the pathlines and their distance when seeded from the same positions.

5. Results

In this section, we validate our method by comparing it to measured data, linear interpolation and the forward-only simulation method by de Hoon et al. [dHvPJV14]. Due to the lack of a ground truth for PC-MRI data, it is difficult to validate any interpolation method. To circumvent this, we use both synthetic and measured data. Experiments considering robustness to noise were performed by de Hoon et al. Our method does not add any variation to their analysis, therefore, robustness is omitted here.

5.1. Synthetic flow comparison

Due to the lack of analytical formulations for complex 3D flows, it is difficult to generate realistic synthetic flow data for the validation of measured flow. Yet, to test the interpolation, one can use synthetic data to analyse certain characteristics. In this paper, we use an irrotational vortex in a spherical mesh with increasing velocity over time $t \in [0,3]$ defined by velocity $\mathbf{u} = (u,v,w)$ for a position $\mathbf{x} = (x,y,z)$, where x, y and z are in the range $[-1,1]$:

$$\begin{cases} scale_r = \max(0.7 - \sqrt{x^2+y^2+z^2}, 0) \\ scale_t = t \cdot 20 + 40 \\ u^t(\mathbf{x}) = scale_r \cdot scale_t \cdot \dfrac{y}{\sqrt{x^2+y^2}} \\ v^t(\mathbf{x}) = scale_r \cdot scale_t \cdot \dfrac{-x}{\sqrt{x^2+y^2}} \\ w^t(\mathbf{x}) = 0, \end{cases} \tag{6}$$

where $scale_r$ scales the magnitude of the flow depending on the position within the spherical mesh and ensures that the velocity is $\mathbf{0}$ at the boundaries of the mesh, thus enforcing the no-slip condition; $scale_t$ is used to increase the flow magnitude over time. At the grid centre, the formula above is not valid, hence, we set the velocity to $\mathbf{0}$. Figure 3 shows three slices of the synthetic flow described above. For this synthetic data, the exact flow is known for every given point

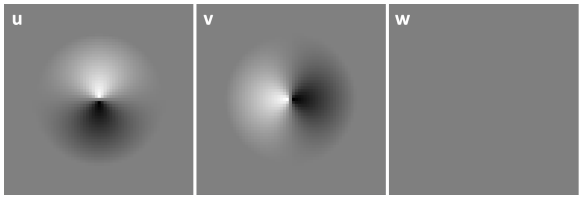

Figure 3: Three slices of the synthetic irrotational vortex flow in a sphere, showing the three velocity components (u, v and w) given by Equation (6).

in time, hence a ground truth exists. Given the lack of a complex analytical flow description, in this special case, linear interpolation would estimate the flow perfectly. However, the purpose of this analysis is to compare the general behaviour of our algorithm and de Hoon et al. [dHvPJV14]. Figure 4 shows the average magnitude over time for the method by de Hoon et al. and our method. The method by de Hoon et al. shows clear discontinuities in average magnitude values, with maxima just before being coupled to new synthetic-data samples (measurements). On the contrary, our method circumvents this issue and shows much smaller deviations from the computed average magnitude. This example illustrates the theoretical advantages of using the bidirectional method, but does not show the characteristics of the method in real data.

5.2. Measured flow comparison

We also evaluated our method using reconstructed high temporal resolution PC-MRI data with no additional processing applied. Figure 5 shows three slices of this data set. The data has a higher temporal and spatial resolution compared to commonly used PC-MRI measurements, as one velocity component was obtained per acquisition, instead of all three components in a single acquisition. Consequently, the acquisition time is significantly higher, making it less suitable for clinical practice. 46 phases were measured covering a single heartbeat, while customary PC-MRI measurements

© 2016 The Author(s)
Eurographics Proceedings © 2016 The Eurographics Association.

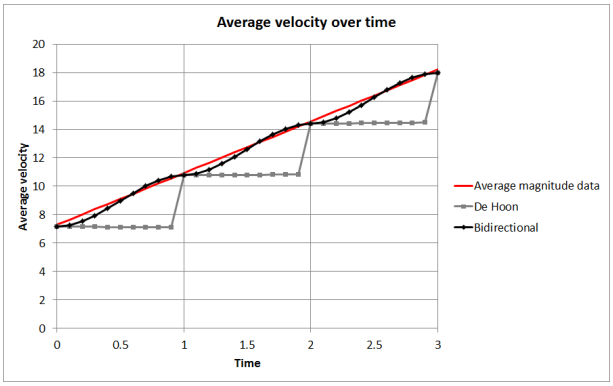

Figure 4: Using a synthetic irrotational vortex flow in a sphere with increasing magnitude over time, we compare the average magnitude of the flow for both our bidirectional method (black) and the method by de Hoon et al. [dHvPJV14] (grey) to the average magnitude cm/s computed from the data (red).

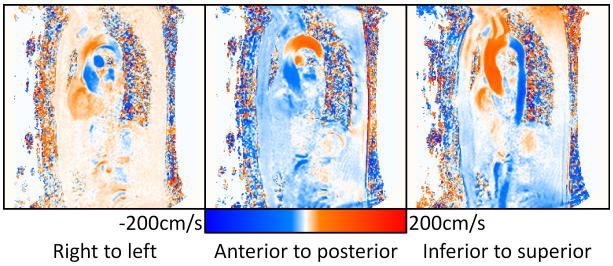

Figure 5: Three PC-MRI slices at peak systole showing the three measured velocity components. Blue and red respectively represent negative and positive values, while black indicates values near zero.

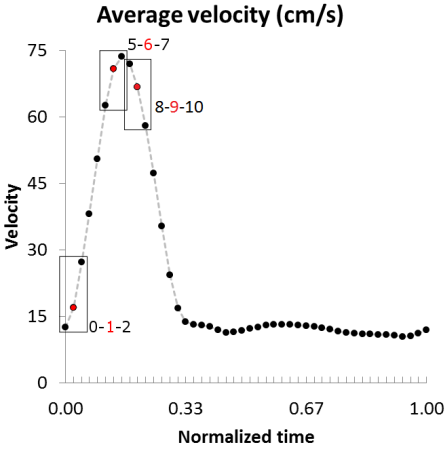

Figure 6: Every dot represents the average velocity inside the mesh per measurement. The time is normalized over a total of 46 measurements. The boxes represent the selection of measurements used per evaluation and the index of the selected measurements. The red dot represents the measurement that was left out, see text.

yield 20 to 25 phases per heart cycle. This high temporal resolution of 23ms is obtained on a Philips Ingenia MRI using the Turbo Field Echo Phase Imaging (TFEPI) protocol. The average measured velocity throughout the volume per phase is given in Figure 6. The three separate acquisitions of the velocity components resulted in three scalar volumes representing a single vector volume of $256 \times 256 \times 22$ voxels sized $1.5625 \times 1.5625 \times 2.5$mm. Measurements were performed with resporitatory gating, a velocity encoding (venc) of 2m/s, a repetition time (TR) of 5.807ms, an echo time (TE) of 3.029ms and a flip angle of 10°. A mesh was derived from the temporal maximum intensity projection (tMIP), using the vascular modelling toolkit software (vmtk) [APB*08].

For a qualitative and quantitative analysis of our method, we compare the result with the high-resolution measured data of a healthy volunteer. This **measured** flow is directly compared with linear interpolation (**Lerp**), forward simulation as proposed by **de Hoon** [dHvPJV14] and our **bidirectional** approach. Removing a measurement allows us to compare interpolated data with the left out measurement, while still maintaining a resolution close to common PC-MRI scans. We analyse both locally and globally the differences based on the metrics given in Table 1. Furthermore, we compare the volumetric flow rate through three slices shown in Figure 2, situated in the ascending aorta, the aortic arc and the descending aorta. We found that the divergence of simulated flow field is 0, and therefore, a comparison will not bring much relevant information.

We focus on the systole, which is the period of high magnitude flow in the aorta due to the contraction of the heart, and hence has a high signal to noise ratio (SNR). In Figure 6 the systole is the first $1/3$ of the cardiac cycle with a period of roughly 300ms.

Three subsets of the measured data were used, namely 0-1-2, 5-6-7 and 8-9-10 where respectively, measurement 1, 6 and 9 were left out for comparisons with the interpolation methods, see Figure 6. Other phases could be used, but these were selected since they represent the behaviour of the methods when dealing with increasing magnitude of the flow for different magnitudes. For decreasing magnitude of flow velocity, the methods behave overall similarly. However, when the damping of the forward simulation produces a result comparable to the measured flow, our method may yield a more deviating result, as shown in Figure 7. In this case, our method slightly underestimates the velocity magnitude by taking measurement 10 into account.

For subset 0-1-2 the SNR is relatively low, since the flow magnitude is low, especially in the aortic arch and descending aorta. This results in more variation in the metrics, such as, the velocity and acceleration in the descending aorta. The coupled flow reduces this unexpected variation, however, since the flow velocity is increasing over time, the forward-only simulation does not interpolate the acceleration correctly due to the bias towards measurement 0. Figure 7 shows this bias is clearly present in the ascending aorta.

For subset 5-6-7, a clear laminar flow pattern is expected. The velocity of the flow is parallel to the walls and the speed varies from zero at the walls to a maximum at the centerline of the vessel. This flow pattern is evident in the high-velocity measured flow, however, the coupled flow enhances it, as shown in Figure 7. Furthermore,

© 2016 The Author(s)
Eurographics Proceedings © 2016 The Eurographics Association.

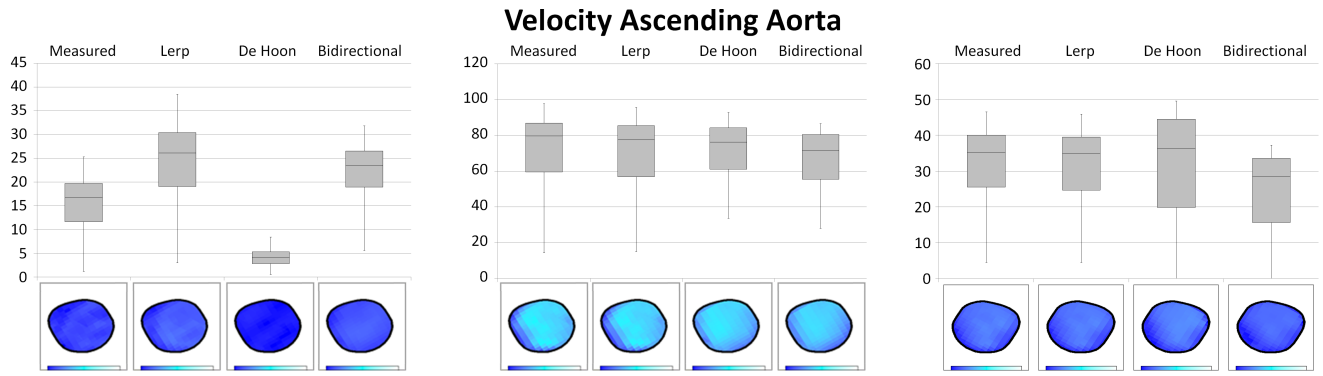

Figure 7: Box plots of the velocity in cm/s for the ascending aorta and the corresponding cross section for each method are shown. The results for left-out measurements 1, 6 and 9 (left to right) are shown. The velocity magnitude is similar for all methods, except the method by De Hoon et al. [dHvPJV14] when the velocity is increasing, as shown by left-out measurement 1. Furthermore, the coupled methods show less variation and a more pronounced laminar flow pattern compared to the measured and linearly interpolation flow. In each image the color coding encodes velocity magnitude in the range 0 to 200cm/s.

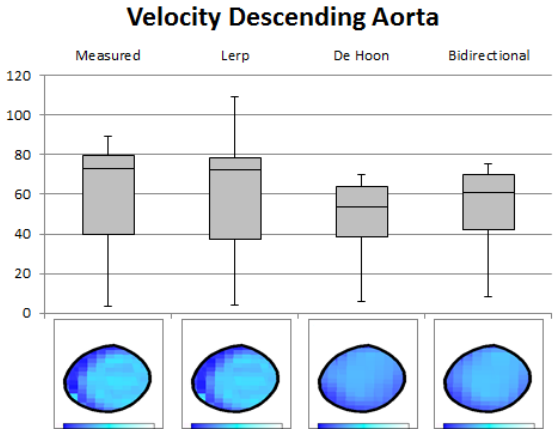

Figure 8: Box plots of the velocity in cm/s for the descending aorta and the corresponding cross section for each method are shown. The results for measurement 6 are shown. Both the measured and linearly interpolated cross sections show a high velocity in one of the lower left voxels, likely a consistent artifact. The coupled methods do not show a high velocity for this voxel. In each image the color coding encodes velocity magnitude in the range 0 to 200cm/s.

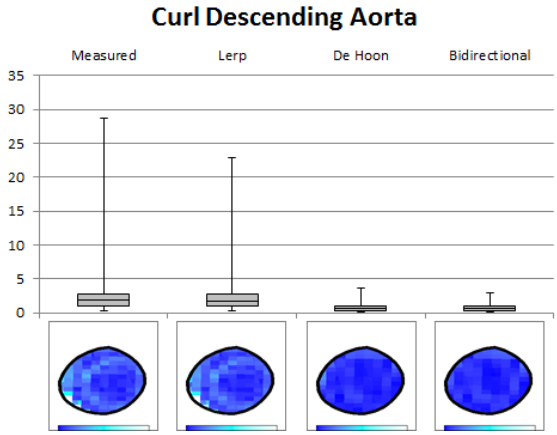

Figure 9: Box plots of the curl in cm/s for the descending aorta and the corresponding cross section for each method are shown. The results for measurement 6 are shown. For this measurement the flow is expected to be laminar, and thus, a low value or zero local curl is expected. In each image the color coding encodes curl magnitude in the range 0 to 15cm/s.

consistent artifacts are corrected using the coupling, while they remain present in the linearly-interpolated result, as shown by Figure 8.

Overall, the coupling reduces the local curl significantly. This local curl represents local vorticity per voxel, and most likely is due to noise or artifacts. Especially in laminar flow, which has flow parallel to the vessel wall, low or zero curl is expected. An example of the reduction in curl by the coupling methods is shown in Figure 9. It shows the curl in the descending aorta for subset 5-6-7.

Our method still suffers from damping effects, although less, compared to forward-only simulation, as shown in Figure 8. Also, in some cases our method results in an overestimation of the acceleration, visible in Figure 10. However, it is clearly closer to the measured flow than the method by De Hoon et al. [dHvPJV14].

Figure 11 shows the WSS for measurement 6. Naturally, by using the no-slip boundary condition, the simulation reduces the WSS. Furthermore, the estimated WSS of the measurements can partially be elicited by motion artifacts and segmentation errors, which are reduced by the coupled flow. Thus, the estimates for the WSS, are lower, however, the higher WSS is present in the expected regions, especially in the inner and outer arch.

Figure 12 shows the global flow for both linearly interpolated flow and bidirectionally simulated flow in subset 0-1-2, in which

© 2016 The Author(s)
Eurographics Proceedings © 2016 The Eurographics Association.

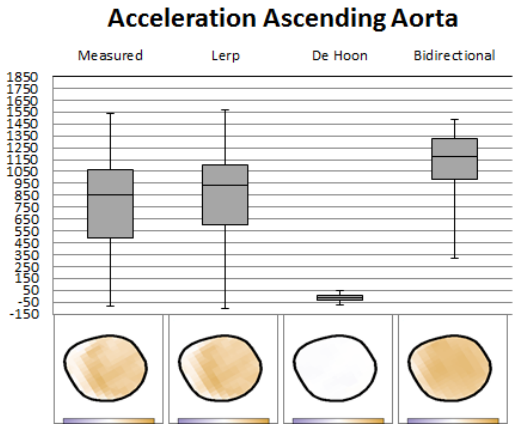

Figure 10: Box plots of the acceleration in cm/s^2 for the ascending aorta and the corresponding cross section for each method are shown. The results for measurement 1 are shown. The bidirectional method overestimates the acceleration, although it is closer to the measured acceleration than the method by De Hoon et al. [dHvPJV14]. In each image the color coding encodes acceleration in the range -2000 to 2000cm/s^2.

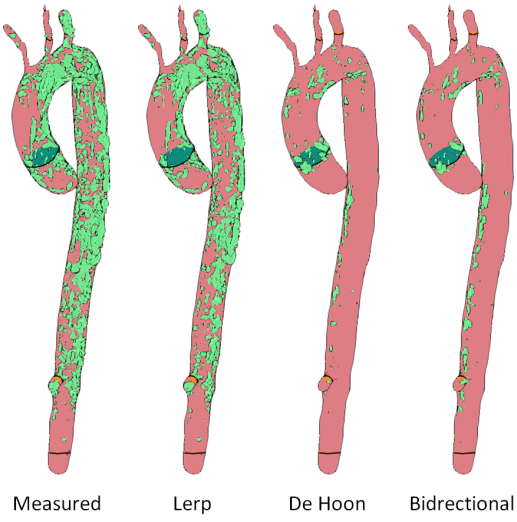

Figure 11: Iso-surfaces enclosing regions of high wall shear stress for left out measurement 6. In the simulated flow less regions are present, indicating a lower over WSS, amongst other causes, due to the implementation of the no-slip boundary condition.

the SNR is low. Clearly, the measured flow is subject to noise and artifacts, which are less apparent in the coupled flow.

The effect of the interpolation on visualizations through time can also be seen in Figure 13. It shows the resulting pathlines for both linearly interpolated and coupled flow fields using Runge-Kutta 4 after a few interpolation steps. The influence of noise and artifacts is visibly reduced, furthermore, the flow has a more laminar pattern.

In Figure 14 the flow of a patient with an aortic dissection is

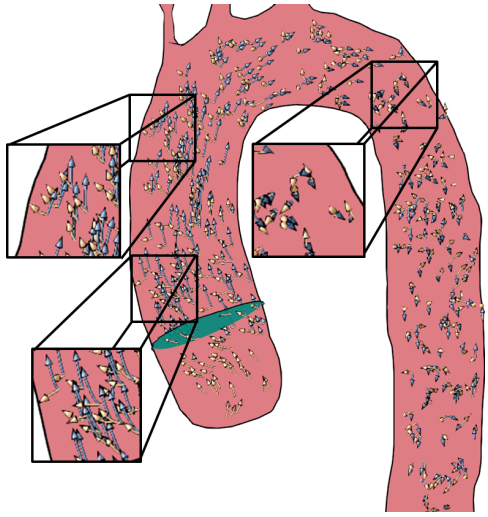

Figure 12: Flow comparison for left out measurement 1 in yellow and the corresponding bidirectionally simulated flow in blue. Measurement 1 has a low signal to noise ratio, this noise is less apparent in the coupled flow.

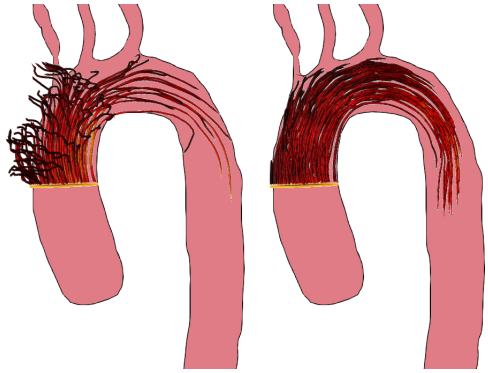

Figure 13: Comparison of using linear interpolation (left) and our technique (right) for pathline visualization. The pathlines are seeded at the ring in the ascending aorta and were advected through the flow over time. The pathlines were computed using Runge-Kutta 4. Our technique provides a more laminar flow pattern and the effect of noise and artifacts is visibly reduced.

shown. An aortic dissection occurs when a tear the inner layer of the aorta wall causes blood to flow between these layers of the wall of the aorta, resulting in a seperation of the layers. In this case, both the flow and the anatomy deviate from the healthy case. A vortex forms in the aortic arch, Figure 14 shows its presence in both the measured and the coupled flow, demonstrating that our method preserves important flow features. Each of the 25 phases of aortic dissection data consists of a vector volume of $144 \times 144 \times 60$ voxels sized $2.0 \times 2.0 \times 2.5$mm. Acquisition was performed with a velocity encoding (venc) of 2m/s, repetition time (TR) of 4.7ms, echo time (TE) 2.7ms, and flip angle of 5°.

© 2016 The Author(s)
Eurographics Proceedings © 2016 The Eurographics Association.

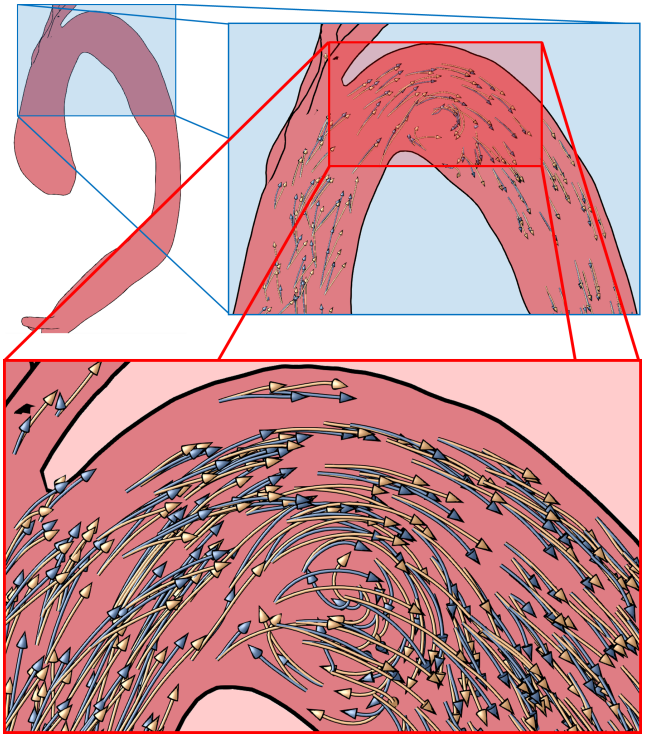

Figure 14: Important flow features, such as vortices, are maintained by our technique. Here, abbarent flow in a patient with an aortic dissection is shown. Yellow pathlines indicate the measured flow, while blue represents the coupled flow.

6. Conclusions and Future work

PC-MRI acquisitions of 4D blood flow are prone to artifacts, while fluid simulations are prone to uncertain model assumptions. Data assimilation can benefit from both measurements and simulations, and subsequently, it can improve the visual and analytical exploration of haemodynamics. We applied the full measured 4D PC-MRI blood-flow velocity data and the physical limitations as imposed by the simulation. The utilisation of the difference of the measured and simulated data yields physically-based velocity fields also between the measured data, improving the temporal resolution, as shown by de Hoon et al. [dHvPJV14]. Moreover, combining measurement and simulation, acquisition artifacts and noise are reduced, resulting in a more laminar flow pattern. By simulating flow in a bidirectional manner, forward and backwards through time, the previously-occurring interpolation bias is evaded. The addition of sources and sinks, as well as the bidirectional simulation, reduces the simulation damping over time.

We evaluated our method, using synthetic flow data and high resolution measurements, to assess the interpolation quality, comparing for velocity magnitude, curl magnitude, acceleration and WSS magnitude. The measurements, albeit having a high resolution, were not of high enough quality for a direct comparison since they still clearly contained noise and artifacts. The flow was shown to be more coherent and to have a more laminar pattern with less outliers than linear interpolation. Furthermore, we have shown that using the bidirectional simulation approach is beneficial for the interpolation quality compared to forward-only simulation, which was already shown to be robust to noise and artifacts [dHvPJV14]. We also illustrated improvement on the visualization due to the interpolation. However, several issues still remain unsolved.

A more advanced data assimilation approach, taking the error of the measurement and the model into account, such as 4-dimensional variational assimilation (4D-Var), could be elaborated on in the future. Such an approach can, in theory, handle the physical limitations of the model, whilst taking the measurement and its local quality into consideration. For such an approach, it is crucial to estimate the local error of PC-MRI data.

Another future direction is to include a time-varying pulsatile mesh based on anatomical measurements to improve both the visual analysis and the quality of the interpolation. This approach would also reduce the uncertainty of the boundary mesh, at the cost of additional data acquisition.

Eventually, the coupling could be applied in clinical practice for treatment planning, e.g., the placement of a stent or valve. Due to the use of a computer-graphics fluid simulation, the fast computation time would allow for a relatively fast inspection of multiple options to determine the influence of the procedure on the haemodynamics. Currently, due to unoptimized code, the bidirectional simulation takes a few hours for the full hearth cycle on average consumer hardware. Optimization of the code can potentially improve the performance greatly. Ideally, the interpolation should be performed on the fly. Yet, when higher compution times are permitted the use of more conventional CFD simulations could be considered and compared to.

Evaluation remains a difficult task due to the lack of ground truth. Finding good strategies to evaluate the results of algorithms for blood flow PC-MRI data as the ones presented in this paper remains ongoing research. The use of more data sets, for example, would allow for statistic analyses of the results.

In conclusion, we extended the approach by de Hoon et al [dHvPJV14], reducing the damping and removing the interpolation bias. Present research suggests, that the combination of 4D PC-MRI velocity data with fluid simulation shows advantages for the understanding of haemodynamics.

Acknowledgments

The patient 4D MRI blood-flow data presented in this article was provided courtesy of the division of Imaging Sciences, King's College Londen at St Thomas' hospital.

References

[AABDZ14] ALIMOHAMMADI M., AGU O., BALABANI S., DÍAZ-ZUCCARINI V.: Development of a patient-specific simulation tool to analyse aortic dissections: Assessment of mixed patient-specific flow and pressure boundary conditions. *Medical Engineering & Physics 36*, 3 (2014). doi:10.1016/j.medengphy.2013.11.003. 2

[APB*08] ANTIGA L., PICCINELLI M., BOTTI L., ENE-IORDACHE B., REMUZZI A., STEINMAN D.: An image-based modeling framework for patient-specific computational hemodynamics. *Medical & Biological Engineering & Computing 46*, 11 (2008), 1097–1112. URL:

© 2016 The Author(s)
Eurographics Proceedings © 2016 The Eurographics Association.

http://dx.doi.org/10.1007/s11517-008-0420-1, doi:10.1007/s11517-008-0420-1. 6

[BEE*15] BOCQUET M., ELBERN H., ESKES H., HIRTL M., ŽABKAR R., CARMICHAEL G., FLEMMING J., INNESS A., PAGOWSKI M., PÉREZ CAMAÑO J., SAIDE P., JOSE R. S., SOFIEV M., VIRA J., BAKLANOV A., CARNEVALE C., GRELL G., SEIGNEUR C.: Data assimilation in atmospheric chemistry models: current status and future prospects for coupled chemistry meteorology models. *Atmospheric Chemistry and Physics 15*, 10 (2015), 5325–5358. doi:10.5194/acp-15-5325-2015. 2

[BMGS13] BORN S., MARKL M., GUTBERLET M., SCHEUERMANN G.: Illustrative visualization of cardiac and aortic blood flow from 4D MRI data. In *Visualization Symposium (PacificVis), 2013 IEEE Pacific* (2013), pp. 129–136. doi:10.1109/PacificVis.2013.6596137. 1

[Bri08] BRIDSON R.: *Fluid Simulation for Computer Graphics*. A.K. Peters, 2008. 2

[DHH*16] DORNIAK K., HEIBERG E., HELLMANN M., RAWICZ-ZEGRZDA D., WESIERSKA M., GALASKA R., SABISZ A., SZUROWSKA E., DUDZIAK M., HEDSTRÖM E.: Required temporal resolution for accurate thoracic aortic pulse wave velocity measurements by phase-contrast magnetic resonance imaging and comparison with clinical standard applanation tonometry. *BMC Cardiovascular Disorders 16*, 1 (2016), 1–9. URL: http://dx.doi.org/10.1186/s12872-016-0292-5, doi:10.1186/s12872-016-0292-5. 2

[dHvPJV14] DE HOON N., VAN PELT R., JALBA A., VILANOVA A.: 4D MRI flow coupled to physics-based fluid simulation for blood-flow visualization. *Computer Graphics Forum 33*, 3 (2014), 121–130. doi:10.1111/cgf.12368. 2, 3, 4, 5, 6, 7, 8, 9

[DN15] DOYLE B., NORMAN P.: Computational biomechanics in thoracic aortic dissection: Today's approaches and tomorrow's opportunities. *Annals of Biomedical Engineering* (2015), 1–13. doi:10.1007/s10439-015-1366-8. 1

[DOW08] DUPONCHEEL M., ORLANDI P., WINCKELMANS G.: Time-reversibility of the Euler equations as a benchmark for energy conserving schemes. *Journal of Computational Physics 227*, 19 (2008), 8736–8752. doi:10.1016/j.jcp.2008.06.020. 2, 3

[DPV12] D'ELIA M., PEREGO M., VENEZIANI A.: A variational data assimilation procedure for the incompressible Navier-Stokes equations in hemodynamics. *Journal of Scientific Computing 52*, 2 (2012), 340–359. URL: 10.1007/s10915-011-9547-6, doi:10.1007/s10915-011-9547-6. 2

[HBB*10] HIRATZKA L., BAKRIS G., BECKMAN J., BERSIN R., CARR V., CASEY JR D., EAGLE K., HERMANN L., ISSELBACHER E., KAZEROONI E., KOUCHOUKOS N., LYTLE B., MILEWICZ D., REICH D., SEN S., SHINN J., SVENSSON L., WILLIAMS D.: Guidelines for the diagnosis and management of patients with thoracic aortic disease. *Journal of the American College of Cardiology 55*, 14 (2010), 27–129. doi:10.1016/j.jacc.2010.02.015. 1

[HMM*10] HEYS J., MANTEUFFEL T., MCCORMICK S., MILANO M., WESTERDALE J., BELOHLAVEK M.: Weighted least-squares finite elements based on particle imaging velocimetry data. *Journal of Computational Physics 229*, 1 (2010), 107–118. doi:10.1016/j.jcp.2009.09.016. 2

[KGP*13] KÖHLER B., GASTEIGER R., PREIM U., THEISEL H., GUTBERLET M., PREIM B.: Semi-automatic vortex extraction in 4D PC-MRI cardiac blood flow data using line predicates. *TVCG 19*, 12 (2013), 2773–2782. doi:10.1109/TVCG.2013.189. 1

[LGP14] LAWONN K., GASTEIGER R., PREIM B.: Adaptive surface visualization of vessels with animated blood flow. *Computer Graphics Forum 33*, 8 (2014), 16–27. doi:10.1111/cgf.12355. 1

[MBG*15] MOZAFFARIAN D., BENJAMIN E., GO A., ARNETT D., GLAHA M., CUSHMAN M., DE FERRANTI S., DESPRÃL'S J., FULLERTON H., HOWARD V., MUFFMAN M., JUDD S., KISSELA B., LACKLAND D., LICHTMAN J., LISABETH L., LIU S., MACKEY R., MATCHAR D., MCGUIRE D., 3RD E. M., MOY C., MUNTNER P., MUSSOLINO M., NASIR K., NEUMAR R., NICHOL G., PALANIAPPAN L., PANDEY D., REEVES M., RODRIQUEZ C., SORLIE P., STEIN J., TOWFIGHI A., TURAN T., VIRANI S., WILLEY J., WOO D., YEH R., TURNER M.: Heart disease and stroke statistics–2015 update: a report from the American Heart Association. *Circulation 131*, 4 (2015), 29–322. doi:10.1161/CIR.0000000000000152. 1

[MFK*12] MARKL M., FRYDRYCHOWICZ A., KOZERKE S., HOPE M., WIEBEN O.: 4D flow MRI. *Journal of Magnetic Resonance Imaging 36*, 5 (2012), 1015–1036. doi:10.1002/jmri.23632. 1

[MNvTK*16] MORRIS P., NARRACOTT A., VON TENGG-KOBLIGK H., SOTO D. S., HSIAO S., LUNGU A., EVANS P., BRESSLOFF N., LAWFORD P., HOSE D., GUNN J.: Computational fluid dynamics modelling in cardiovascular medicine. *Heart 102*, 1 (2016), 18–28. doi:doi:10.1136/heartjnl-2015-308044. 1

[MSW*16] MARKL M., SCHNELL S., WU C., BOLLACHE E., JARVIS K., BARKER A., ROBINSON J., RIGSBY C.: Advanced flow MRI: emerging techniques and applications. *Clinical Radiology 71*, 8 (2016), 779–795. Special Issue: Spotlight on Cardiovascular Imaging. doi:10.1016/j.crad.2016.01.011. 1

[RHJ*04] RODELL M., HOUSER P., JAMBOR U., GOTTSCHALCK J., MITCHELL K., MENG C.-J., ARSENAULT K., COSGROVE B., RADAKOVICH J., BOSILOVICH M., ENTIN J., WALKER J., LOHMANN D., TOLL D.: The global land data assimilation system. *Bulletin of the American Meteorological Society 85* (2004), 381–394. doi:10.1175/BAMS-85-3-381. 2

[RMB*14] RAJARAMAN P., MANTEUFFEL T., BELOHLAVEK M., MCMAHON E., HEYS J.: Echocardiographic particle imaging velocimetry data assimilation with least square finite element methods. *Computers and Mathematics with Applications 68*, 11 (2014), 1569–1580. doi:10.1016/j.camwa.2014.07.026. 2

[RNNC15] RISPOLI V., NIELSEN J., NAYAK K., CARVALHO J.: Computational fluid dynamics simulations of blood flow regularized by 3D phase contrast MRI. *BioMedical Engineering OnLine 14*, 1 (2015), 1–23. URL: http://dx.doi.org/10.1186/s12938-015-0104-7, doi:10.1186/s12938-015-0104-7. 2

[SBF*14] SCHNEIDER U., BECKER A., FINGER P., MEYER-CHRISTOFFER A., ZIESE M., RUDOLF B.: GPCC's new land surface precipitation climatology based on quality-controlled in situ data and its role in quantifying the global water cycle. *Theoretical and Applied Climatology 115*, 1-2 (2014), 15–40. doi:10.1007/s00704-013-0860-x. 2

[VPvP*12] VILANOVA A., PREIM B., VAN PELT R., GASTEIGER R., NEUGEBAUER M., WISCHGOLL T.: Visual exploration of simulated and measured blood flow. *CoRR abs/1209.0999* (2012). URL: http://arxiv.org/abs/1209.0999. 1

[VPvP*14] VILANOVA A., PREIM B., VAN PELT R., GASTEIGER R., NEUGEBAUER M., WISCHGOLL T.: Visual exploration of simulated and measured blood flow. In *Scientific Visualization*, Hansen C., Chen M., Johnson C., Kaufman A., Hagen H., (Eds.), Mathematics and Visualization. Springer London, 2014, pp. 305–324. doi:10.1007/978-1-4471-6497-5_25. 1

[ZB05] ZHU Y., BRIDSON R.: Animating sand as a fluid. *ACM Trans. Graph. 24*, 3 (2005), 965–972. doi:10.1145/1073204.1073298. 3

[Zha05] ZHAO H.: A fast sweeping method for Eikonal equations. *Mathematics of Computation 74* (2005), 603–627. doi:10.1090/S0025-5718-04-01678-3. 3, 4

© 2016 The Author(s)
Eurographics Proceedings © 2016 The Eurographics Association.